ARTICLE OPEN

Check for updates

Spin-triplet superconductivity in Weyl nodal-line semimetals

Tian Shang[1,10], Sudeep K. Ghosh[2,10], Michael Smidman[3,10], Dariusz Jakub Gawryluk[4], Christopher Baines[5], An Wang[3], Wu Xie[3], Ye Chen[3], Mukkattu O. Ajeesh[6], Michael Nicklas[6], Ekaterina Pomjakushina[4], Marisa Medarde[4], Ming Shi[7], James F. Annett[8], Huiqiu Yuan[3]✉, Jorge Quintanilla[2]✉ and Toni Shiroka[5,9]✉

Topological semimetals are three dimensional materials with symmetry-protected massless bulk excitations. As a special case, Weyl nodal-line semimetals are realized in materials having either no inversion or broken time-reversal symmetry and feature bulk nodal lines. The 111-family, including LaNiSi, LaPtSi and LaPtGe materials (all lacking inversion symmetry), belongs to this class. Here, by combining muon-spin rotation and relaxation with thermodynamic measurements, we find that these materials exhibit a fully-gapped superconducting ground state, while spontaneously breaking time-reversal symmetry at the superconducting transition. Since time-reversal symmetry is essential for protecting the normal-state topology, its breaking upon entering the superconducting state should remarkably result in a topological phase transition. By developing a minimal model for the normal-state band structure and assuming a purely spin-triplet pairing, we show that the superconducting properties across this family can be described accurately. Our results demonstrate that the 111 materials reported here provide an ideal test-bed for investigating the rich interplay between the exotic properties of Weyl nodal-line fermions and unconventional superconductivity.

npj Quantum Materials (2022)7:35 ; https://doi.org/10.1038/s41535-022-00442-w

INTRODUCTION

Topological materials are at the forefront of current condensed matter and material science research due to their great potential for applications. Among their defining characteristics is the symmetry-protected metallic surface state, arising from a non-trivial bulk topology. Recently, the experimental observation of many topological semimetals has shifted the research focus towards this subclass of topological materials[1,2]. Contrary to Dirac- or Weyl semimetals, which have point-type band crossings, in nodal-line semimetals band crossings occur in the form of lines or rings along special **k**-directions of the Brillouin zone. In this case, near the nodes, the low-energy excitations are nodal-line fermions with rather exotic properties[1,2]. Weyl nodal-line semimetals can be realized in systems lacking inversion symmetry or with broken time-reversal symmetry (TRS), provided the nodal lines that are protected by additional symmetries. Recently, the isostructural noncentrosymmetric 111-type materials LaNiSi, LaPtSi, and LaPtGe have been predicted to be Weyl nodal-line semimetals, protected by nonsymmorphic glide planes[3]. In addition, at low temperatures, all of them become superconductors[4–6].

The breaking of additional symmetries in the superconducting state, besides the global gauge symmetry of the wave function, is a key characteristic of unconventional superconductors[7,8]. The combination of intriguing fundamental physics with far-reaching potential for applications has made unconventional superconductors one of the most investigated classes of materials. Broken time reversal symmetry in the superconducting state, one of the typical indications of unconventional superconductivity (SC), is manifested by the spontaneous appearance of magnetic fields below the superconducting transition temperature T_c[9]. Recently, by using the muon-spin relaxation technique, several noncentrosymmetric superconductors (NCSCs) have been found to break TRS in their superconducting state. Otherwise they appear to exhibit the conventional properties of standard phonon-mediated superconductors[9–14]. In NCSCs, singlet-triplet admixed pairings can be induced by antisymmetric spin-orbit coupling (ASOC), however, ASOC itself cannot break TRS[15,16]. Noncentrosymmetric superconductors also provide a fertile ground for topological superconductivity, with potential applications to topological quantum computing[17–19].

According to electronic band-structure calculations, the ASOC strength increases progressively from LaNiSi to LaPtSi to LaPtGe[3]. Hence, the 111-family of materials is a prime candidate for investigating the relationship between ASOC and unconventional SC with TRS-breaking, here made even more interesting by the interplay with the exotic nodal-line fermions. Recent muon-spin relaxation and rotation (μSR) studies on LaNiSi and LaPtSi reported an enhanced muon-spin relaxation at low temperatures, seemingly an indication of TRS breaking. However, their unusual temperature dependence (here resembling a Curie–Weiss behavior), the lack of any distinct features near T_c[20], and the absence of an additional muon-spin relaxation in LaPtGe (below its T_c)[21], all seem to suggest that TRS is preserved in the superconducting state of these 111 materials. We recall that, in the past, inconsistent μSR results have been also reported in UPt_3[22,23], whose TRS breaking could be independently proved by optical Kerr effect only a decade later[24]. Clearly, it is highly desirable to investigate the 111 materials, too, with other techniques such as the Kerr effect, in order to confirm their TRS breaking. Here, by combining extensive and thorough μSR measurements with detailed theoretical analysis, we show that, contrary to previous reports, all the above 111-type materials spontaneously break TRS

[1]Key Laboratory of Polar Materials and Devices (MOE), School of Physics and Electronic Science, East China Normal University, Shanghai, China. [2]School of Physical Sciences, University of Kent, Canterbury CT2 7NH, UK. [3]Center for Correlated Matter and Department of Physics, Zhejiang University, 310058 Hangzhou, China. [4]Laboratory for Multiscale Materials Experiments, Paul Scherrer Institut, CH-5232 Villigen PSI, Switzerland. [5]Laboratory for Muon-Spin Spectroscopy, Paul Scherrer Institut, CH-5232 Villigen PSI, Switzerland. [6]Max Planck Institute for Chemical Physics of Solids, Nöthnitzer Str.40, 01187 Dresden, Germany. [7]Swiss Light Source, Paul Scherrer Institut, CH-5232 Villigen PSI, Switzerland. [8]H. H. Wills Physics Laboratory, University of Bristol, Tyndall Avenue, Bristol BS8 1TL, UK. [9]Laboratorium für Festkörperphysik, ETH Zürich, CH-8093 Zürich, Switzerland. [10]These authors contributed equally: Tian Shang, Sudeep K. Ghosh, Michael Smidman. ✉email: hqyuan@zju.edu.cn; j.quintanilla@kent.ac.uk; tshiroka@phys.ethz.ch

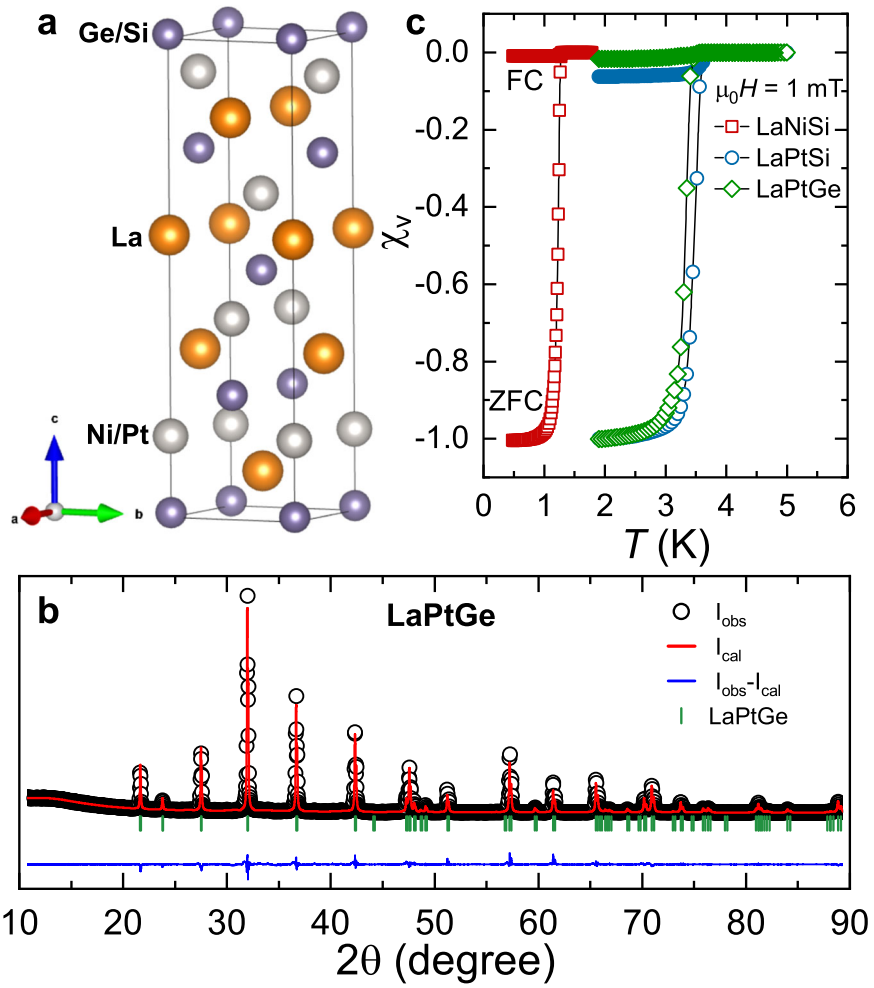

Fig. 1 Crystal structure and bulk superconductivity. a Crystal structure of LaNiSi, LaPtSi, and LaPtGe. **b** Room-temperature XRD pattern and Rietveld refinements for LaPtGe. The black circles and the solid-red line represent the experimental pattern and the Rietveld refinement profile, respectively. The blue line at the bottom shows the residuals, i.e., the difference between calculated and experimental data. The vertical bars mark the calculated Bragg-peak positions for LaPtGe. The Rietveld refinements of LaNiSi and LaPtSi are shown in the Supplementary Fig. 1. **c** Temperature dependence of the magnetic susceptibility. The zero field-cooled (ZFC) and field-cooled (FC) magnetic susceptibility were measured in a field of $\mu_0H = 1$ mT. The well distinct ZFC- and FC curves are consistent with type-II SC, as confirmed also by μSR measurements.

at the superconducting transition and exhibit a fully-gapped pure spin-triplet pairing.

RESULTS

Bulk superconductivity

We synthesized three isostructural LaNiSi, LaPtSi, and LaPtGe samples and investigated systematically their physical properties via magnetic-susceptibility, specific-heat, electrical-resistivity, and μSR measurements. As shown in Fig. 1a, the 111-type materials crystallize in a noncentrosymmetric body-centered tetragonal structure. The corresponding $I4_1md$ space group (No. 109), confirmed by refinements of the powder x-ray diffraction (XRD) patterns (see e.g., in Fig. 1b), is nonsymmorphic and has a Bravais lattice with point group C_{4v} ($4mm$) (see details in Supplementary Note 1 and Table 1). Upon zero-field cooling, full diamagnetic screening (i.e., bulk SC) is found in the magnetic susceptibility measurements in an applied field of 1 mT (Fig. 1c). Consistent with previous studies[4–6], we find $T_c = 1.28$, 3.62, and 3.46 K for LaNiSi, LaPtSi, and LaPtGe, respectively. A prominent specific-heat jump at each superconducting transition (see below) confirms once more the bulk SC nature of these materials.

Lower and upper critical fields

For reliable transverse-field (TF) μSR measurements in a superconductor, the applied magnetic field should exceed the lower critical field H_{c1} and be much less than the upper critical field H_{c2}, so that the additional field-distribution broadening due to the flux-line lattice (FFL) can be quantified from the muon-spin relaxation rate, the latter is directly related to the magnetic penetration depth and thus, to the superfluid density. The H_{c1} values determined from field-dependent magnetization data are summarized in Fig. 2a–c, which provide lower critical fields $\mu_0H_{c1}(0) = 3.9(5)$, 9.6(2), and 11.8 (1) mT for LaNiSi, LaPtSi, and LaPtGe, respectively. These $H_{c1}(0)$ values are fully consistent with those determined from magnetic penetration depth (see below). We investigated also the upper critical fields H_{c2} of these 111 materials, here shown in Fig. 2d–f versus the reduced temperature $T/T_c(0)$ for LaNiSi, LaPtSi, and LaPtGe, respectively. Three different models, including Ginzburg-Landau (GL)[25], Werthamer–Helfand–Hohenberg (WHH)[26], and two-band model[27] were used to analyze the $H_{c2}(T)$ data. In LaNiSi and LaPtGe, $H_{c2}(T)$ is well described by the WHH model, yielding $\mu_0H_{c2}(0) = 0.10(1)$ and 0.44(1) T, respectively. Conversely, in LaPtSi, both WHH and GL models fit $H_{c2}(T)$ reasonably well only at low fields, i.e., $\mu_0H_{c2} < 0.2$ T. At higher magnetic fields, both models

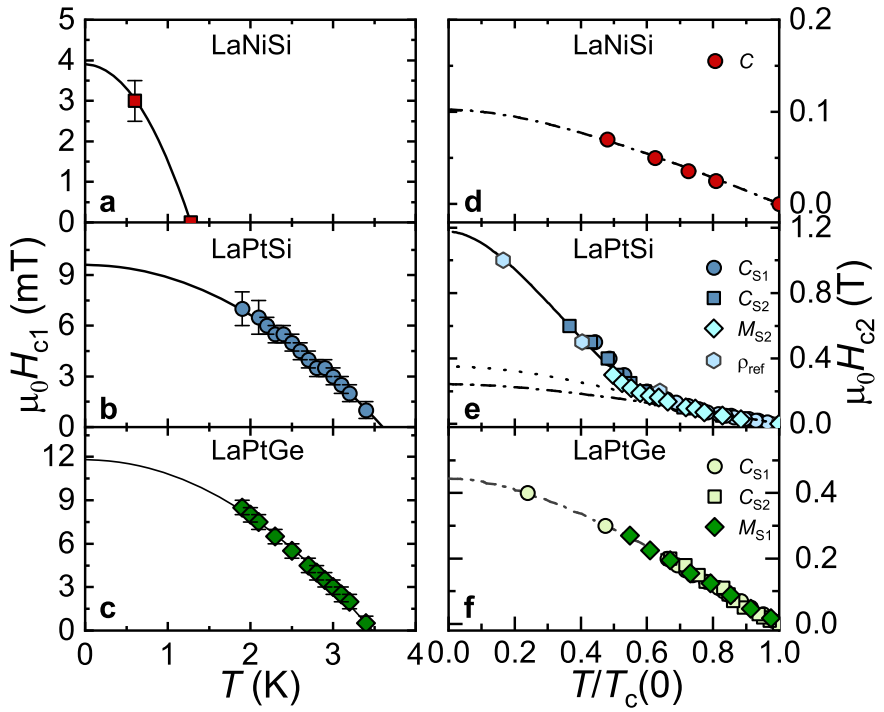

Fig. 2 Lower and upper critical fields. a–c The lower critical fields H_{c1} as a function of temperature for LaNiSi (**a**), LaPtSi (**b**), and LaPtGe (**c**). For each temperature, H_{c1} was determined as the value where the field-dependent magnetization $M(H)$ starts to deviate from linearity (see Supplementary Fig. 3 and Note 3). Solid lines are fits to $\mu_0 H_{c1}(T) = \mu_0 H_{c1}(0)[1-(T/T_c)^2]$. **d–f** Upper critical fields H_{c2} versus the reduced temperature T/T_c for LaNiSi (**d**), LaPtSi (**e**), and LaPtGe (**f**). The superconducting transition temperatures T_c were determined from heat-capacity- $C(T)$ and magnetization measurements $M(H)$ (see details in Supplementary Figs. 4–6 and Note 4). For LaPtSi and LaPtGe, two different sample batches (denoted as S1 and S2) were measured. The dash-dotted-lines, dashed-lines, and solid-lines are fits using WHH-, GL-, and two-band models, respectively. The H_{c2} values determined from $\rho(T,H)$ from ref. [5] are also plotted in **e** for LaPtSi. The error bars of H_{c1} are the field-step values used during the $M(H)$ measurements.

deviate significantly from the experimental data. Such a discrepancy most likely hints at multiple superconducting gaps in LaPtSi, as evidenced also by the positive curvature of $H_{c2}(T)$, a typical feature of multigap superconductors. Indeed, here the two-band model shows a remarkable agreement with the experimental data and provides $\mu_0 H_{c2}(0) = 1.17(2)$ T. The presence of multiple superconducting gaps is also supported by the field-dependent electronic specific-heat coefficient (see Supplementary Fig. 11 and Note 7). However, note that, due to the similar gap sizes (or to small relative weights) of LaPtSi, the multigap features are not easily discernible in the superfluid density or in the zero-field electronic specific heat[28,29].

ZF-μSR and evidence of TRS breaking

Zero-field (ZF)-μSR is a very sensitive method for detecting weak magnetic fields (down to ~0.01 mT[30]) due to the large muon gyromagnetic ratio (851.615 MHz T^{-1}) and to the availability of nearly 100% spin-polarized muon beams. Therefore, the ZF-μSR technique has been successfully used to study different types of unconventional superconductors with broken TRS in their superconducting state[10,11,13,14,22,31–34]. To search for the presence of TRS breaking in the superconducting state of 111 materials, ZF-μSR measurements were performed at various temperatures, covering both their normal- and superconducting states. Representative ZF-μSR spectra are shown in Fig. 3a–c for LaNiSi, LaPtSi, and LaPtGe, respectively. The ZF-μSR spectra exhibit small yet clear differences between 0.02 K and temperatures above T_c (e.g., 1.9 K) for LaNiSi, which become more evident in the LaPtSi and LaPtGe case.

In general, in absence of external magnetic fields, the muon-spin relaxation is mostly determined by the interaction of muon spins with the randomly oriented nuclear magnetic moments. Thus, the ZF-μSR asymmetry can be described by means of a phenomenological relaxation function, consisting of a combination of Gaussian- and Lorentzian Kubo-Toyabe relaxations [see Eq. (2)][35,36]. While $\sigma_{ZF}(T)$ is found to be nearly temperature independent (see Supplementary Fig. 7), as shown in Fig. 3d–f, all three compounds show a clear increase of the muon-spin relaxation in the Λ_{ZF} channel below T_c. Conversely, for $T > T_c$, $\Lambda_{ZF}(T)$ is flat, thus excluding a possible origin related to magnetic impurities (the latter typically follow a Curie–Weiss behavior[28]). Furthermore, longitudinal-field (LF) μSR measurements at base temperature (see Fig. 3a–c) indicate that a field of only 10 mT is sufficient to decouple the muon spins from the TRS breaking relaxation channel in all three compounds, indicating that the weak internal fields are static within the muon lifetime. Furthermore, the LF-μSR results rule out an extrinsic origin for the enhanced $\Lambda_{ZF}(T)$. Considered together, the ZF-μSR and LF-μSR results clearly evidence the increase in $\Lambda_{ZF}(T)$ below T_c with the occurrence of spontaneous magnetic fields[10,11,13,14,22,31–34] and, hence, the breaking of TRS in the superconducting state of LaNiSi, LaPtSi, and LaPtGe.

TF-μSR and nodeless superconductivity

To investigate the superconducting order parameters of LaNiSi, LaPtSi, and LaPtGe, the temperature dependence of their magnetic penetration depth was determined via TF-μSR measurements. The development of a flux-line lattice in the mixed state of a superconductor broadens the internal field distribution and leads to an enhanced muon-spin relaxation rate. Since the latter is determined by the magnetic penetration depth and, ultimately, by the superfluid density, the superconducting order parameter can

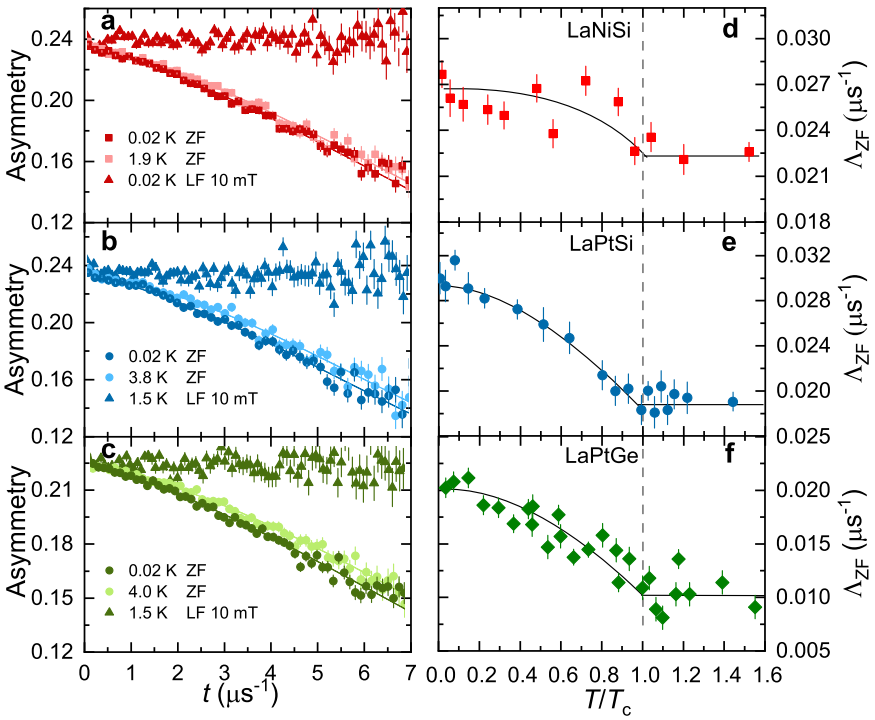

Fig. 3 Probing TRS breaking superconductivity via ZF-μSR. a–c Zero-field μSR spectra collected above and below T_c in LaNiSi (**a**), LaPtSi (**b**), and LaPtGe (**c**). In all cases, the lack of any oscillations implies a lack of long-range magnetic order. Solid lines through the data in **a**–**c** are fits to Eq. (2). The flat μSR datasets in **a**–**c** correspond to LF-μSR spectra, suggesting that even a small longitudinal field is sufficient to decouple muon spins from the local field. **d**–**f** Zero-field muon-spin relaxation rate Λ_{ZF} versus the reduced temperature T/T_c for LaNiSi (**d**), LaPtSi (**e**), and LaPtGe (**f**). Solid lines in **d**–**f** are guides to the eyes. A consistent increase of Λ_{ZF} below T_c reflects the onset of spontaneous magnetic fields, indicative of a breaking of TRS in the superconducting state, while the σ_{ZF} is almost temperature independent (see details in Supplementary Fig. 7 and Note 5). The error bars of Λ_{ZF} are the SDs obtained from fits to Eq. (2) by the `musrfit` software package[52].

be evaluated from the temperature-dependent TF-μSR measurements (see "Methods" section). Following a field-cooling protocol down to 0.02 K, the TF-μSR spectra were collected at various temperatures upon warming, covering both the superconducting and the normal states. As shown in Fig. 4a–c, below T_c, the fast decay in the TF-μSR asymmetry caused by the FLL is clearly visible. By contrast, the weak decay in the normal state, is attributed to the nuclear magnetic moments, being similar to the ZF-μSR in Fig. 3a–c. The TF-μSR spectra were analyzed by means of Eq. (3). Above T_c, the relaxation rate is small and temperature-independent, but below T_c it starts to increase due to the formation of a FLL and the corresponding increase in superfluid density. At the same time, a diamagnetic field shift appears below T_c (see Fig. 4d–f). The effective magnetic penetration depth and the superfluid density were calculated from the measured superconducting Gaussian relaxation rates (see "Methods" section). The normalized inverse-square of the effective magnetic penetration depth $\lambda_{eff}^{-2}(T)$ (proportional to the superfluid density) vs. the reduced temperature T/T_c for LaNiSi, LaPtSi, and LaPtGe is presented in Fig. 4g–i, respectively. Although these three NCSCs exhibit different T_c values and ASOC strengths, below $T_c/3$, their λ_{eff}^{-2} values are practically independent of temperature. The low-T invariance of $\lambda_{eff}^{-2}(T)$ and, consequently, of the superfluid density, clearly suggests the lack of low-energy excitations and, hence, a nodeless superconductivity in LaNiSi, LaPtSi, and LaPtGe, in good agreement with the low-T electronic specific-heat data (see below) and magnetic penetration depth measurements via the tunnel-diode-oscillator technique. The solid lines through the data in Fig. 4g–i are fits using a fully-gapped s-wave model with a single superconducting gap. These yield gap values $\Delta_0 = 1.95(5)$, 1.80 (5), and 2.10(5) k_BT_c, and $\lambda_0 = 300(3)$, 228(3), and 219(2) nm for LaNiSi, LaPtSi, and LaPtGe, respectively. When employing the dirty-limit model we find similar parameters (see Supplementary Fig. 9 and Note 6). The gap values determined via TF-μSR are highly consistent with those derived from the specific-heat measurements (see Supplementary Table 5).

Minimal two-band model and electronic specific heat

The three 111 materials, LaNiSi, LaPtSi, and LaPtGe share similar band structures and are inherently multiband systems, with several orbitals contributing to the density of states (DOS) at the Fermi level[3]. The lack of an inversion center implies that an antisymmetric spin-orbit coupling is naturally present in these materials. Here, the ASOC splits the bands near the Fermi level, with an increasingly larger strength from LaNiSi to LaPtSi to LaPtGe[3]. In their normal state, all of them are nonmagnetic and, thus, preserve TRS. These materials have been predicted to exhibit four Weyl nodal rings around the X point, at ~0.5 eV below the Fermi level, a topological feature protected by nonsymmorphic glide mirror symmetry and TRS[3]. The size of the nodal rings increases with increasing ASOC strength and, due to their presence, the 111-type Weyl nodal-line semimetals are expected to show interesting magneto-transport properties.

The antisymmetric spin–orbit coupling, however, does not change the topology of the Fermi surfaces qualitatively. In the 111 materials, in the absence of ASOC, three spin-degenerate bands cross the Fermi level giving rise to three Fermi surfaces with similar shapes. However, only two of them contribute significantly (~96%) to the DOS at the Fermi level (see Supplementary Fig. 12 and Note 9)[3]. The low-energy properties of 111 materials are thus dominated by these two Fermi surfaces. To capture qualitatively their topology, we construct a minimal two-band tight-binding model by suitably choosing the chemical

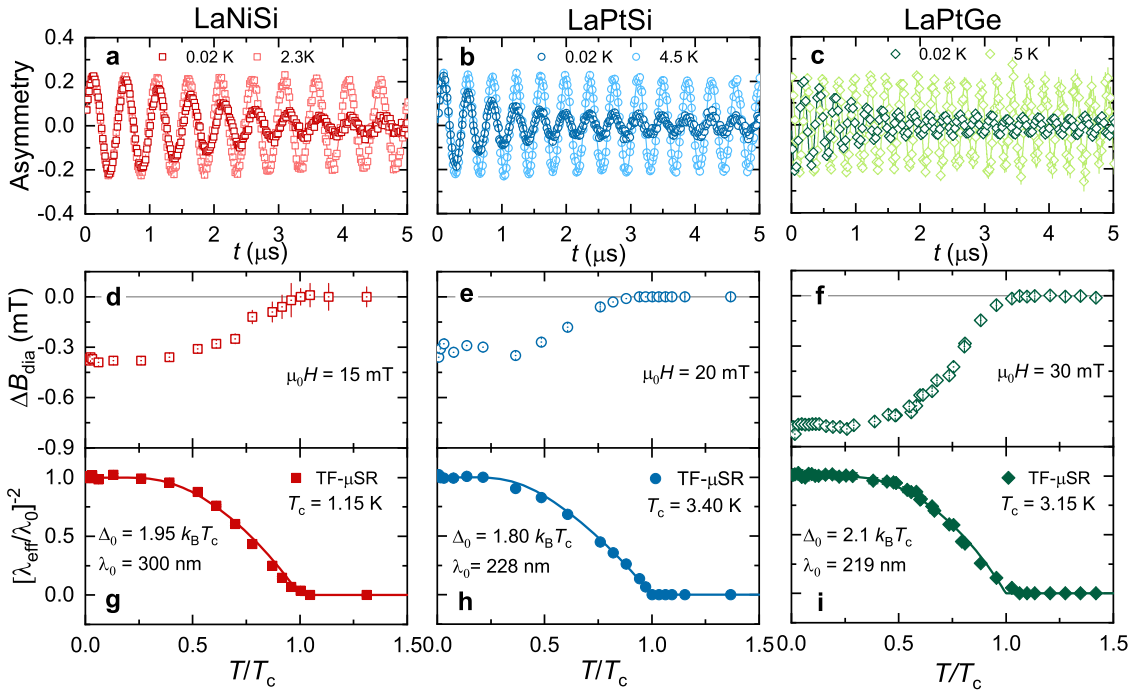

Fig. 4 Exploring the superconducting pairing via TF-μSR. a–c TF-μSR spectra, collected in the superconducting and normal states (i.e., above and below T_c) of LaNiSi (**a**), LaPtSi (**b**), and LaPtGe (**c**). The optimal field values for the TF-μSR measurements were identified from the lower critical field H_{c1} and the field-dependent superconducting relaxation rate (see Fig. 2, Supplementary Fig. 8 and Note 6) and correspond to 15, 20, and 30 mT for LaNiSi, LaPtSi, and LaPtGe, respectively. **d–f** Diamagnetic shift ΔB_{dia} versus the reduced temperature T/T_c for LaNiSi (**d**), LaPtSi (**e**), and LaPtGe (**f**). Here, $\Delta B_{dia} = B_s - B_{appl}$, with B_s the local magnetic field sensed by implanted muons in the sample and B_{appl} the applied magnetic field. Due to the formation of the FLL, a diamagnetic field shift appears below T_c. **g–i** Superfluid density $[\rho_{sc}(T) \propto \lambda_{eff}^{-2}(T)]$ as a function of reduced temperature T/T_c for LaNiSi (**g**), LaPtSi (**h**), and LaPtGe (**i**). Solid lines represent fits to a fully-gapped *s*-wave model. The error bars of $\lambda^{-2}(T)$ are the SDs obtained from fits of the TF-μSR spectra to Eq. (3) by the `musrfit` software package[52].

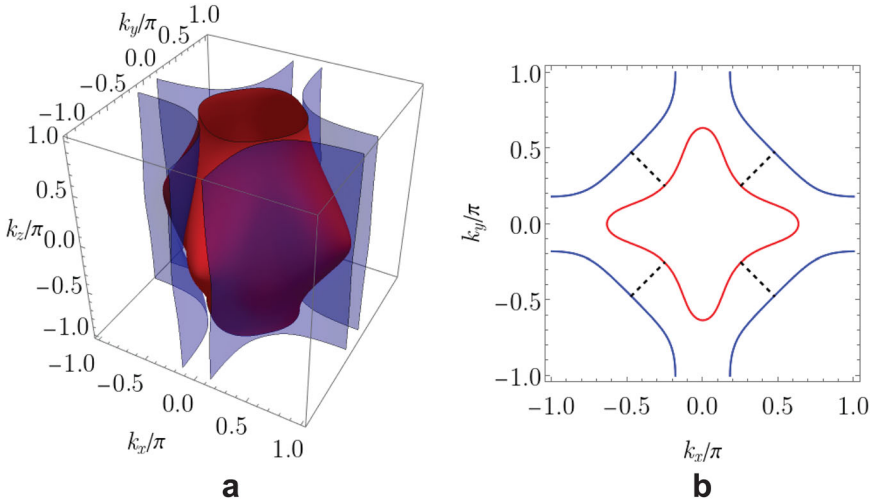

Fig. 5 Fermi surfaces for a minimal two-band model. a, b The two important Fermi surfaces of the 111-type materials can be qualitatively reproduced by a range of parameters in a minimal two-band model. Here, we set $t_{\parallel} = 1$ eV, and use the values (normalized by $t_{\parallel}$): $\mu = -1.5$, $t_{\perp} = 0.70$, $t_d = 1.25$, $t_\delta = 0.60$, $t_m = 0.40$, $\varepsilon_1^{(0)} = 0.45$, and $\varepsilon_2^{(0)} = -0.20$. The two corresponding Fermi surfaces are shown in **a**, while their projections on the $k_z = 0$ plane are shown in **b**. The dashed lines in **b** depict schematically the interband nature of the pairing of electrons.

potential. The dispersions of the two bands are:

$$\epsilon_j(\mathbf{k}) = \varepsilon_j^{(0)} + g_1(\mathbf{k}) + (-1)^j g_2(\mathbf{k}), \quad (1)$$

where $j = 1, 2$; $\varepsilon_j^{(0)}$ are the onsite energies, $g_1(\mathbf{k}) = [\epsilon'(\mathbf{k}) + \epsilon''(\mathbf{k})]/2$, $g_2(\mathbf{k}) = [\{\epsilon'(\mathbf{k}) - \epsilon''(\mathbf{k})\}^2/4 + t_m^2]^{1/2}$, with $\epsilon'(\mathbf{k}) = [\epsilon(k_x) + \epsilon(k_y)]/2 - [\{\epsilon(k_x) - \epsilon(k_y)\}^2/4 + t_\delta^2]^{1/2}$, $\epsilon(x) = -2t_{\parallel}\cos(x)$, $\epsilon''(\mathbf{k}) = -2t_{\perp}\cos(k_z) - 2t_d[\cos(k_x) + \cos(k_y)]$. Here, $t_{\parallel}$, t_m, t_d, t_δ, and $t_{\perp}$ are the hopping parameters. The corresponding Fermi surfaces for a realistic choice of the parameters—to be used in the subsequent discussion—are shown in Fig. 5a.

To account for the ASOC effects in the minimal two-band model, we note that the form of ASOC for the corresponding C_{4v} point group is $V_{ASOC} = \alpha_{xy}(k_y\sigma_x - k_x\sigma_y) + \alpha_z k_x k_y k_z(k_x^2 - k_y^2)\sigma_z$, where $\boldsymbol{\sigma} = (\sigma_x,$

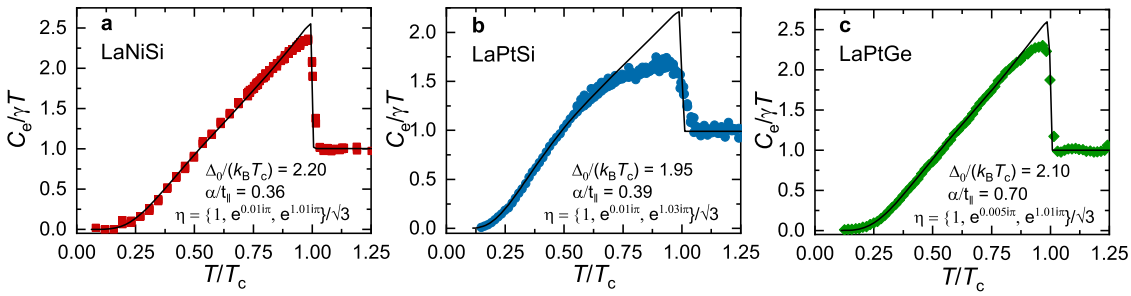

Fig. 6 Electronic specific heat. a–c Normalized electronic specific heat $C_e/\gamma T$ (with γ the normal-state electronic specific-heat coefficient) as a function of the reduced temperature T/T_c for LaNiSi (**a**), LaPtSi (**b**), and LaPtGe (**c**). C_e/T was determined by subtracting the phonon contribution from the raw specific-heat data (see Supplementary Fig. 10 and Note 7). Solid lines through the data represent theoretical calculations corresponding to the INT state with the fit parameters listed in the figures. For LaPtSi, the reduced specific-heat jump at T_c is mostly caused by the broadening of the superconducting transition.

σ_y, σ_z) is the vector of Pauli matrices in the spin space, while α_{xy} and α_z are the strengths of the two types of ASOC terms allowed by symmetry[15]. Note that, the second term is of fifth order in k and leads to spin splitting. On the other hand, the Rashba term, with strength α_{xy}, is expected to be dominant because of the quasi-2D nature of the two Fermi surfaces (see Fig. 5a). Hence, only the Rashba ASOC term is phenomenologically relevant in the minimal model. In general, this term would have both interband and intraband contributions. However, to maintain the topology of the Fermi surfaces in presence of ASOC similar to that in its absence and to correctly describe the experimental observations in the 111 materials, we need to work in the limit where the interband contribution is large compared to the intraband one (see Supplementary Table 2 and Note 8 for details). This emphasizes the interband nature of the pairing under consideration. As a result, we only consider an interband Rashba ASOC of strength α, i.e., $V_R^{\text{inter}} = \alpha(k_y\sigma_x - k_x\sigma_y)$. The normal-state Hamiltonian then takes the form $\hat{\mathcal{H}}_N = \sum_{\mathbf{k}} \hat{c}_{\mathbf{k}}^{\dagger} \cdot H_N(\mathbf{k}) \cdot \hat{c}_{\mathbf{k}}$, where $H_N(\mathbf{k}) = \sigma_0 \otimes \begin{bmatrix} \xi_1(\mathbf{k}) & 0 \\ 0 & \xi_2(\mathbf{k}) \end{bmatrix} + \alpha(k_y\sigma_x - k_x\sigma_y) \otimes \tau_x$. Here, $\xi_j(\mathbf{k}) = \epsilon_j(\mathbf{k}) - \mu$, with μ being the chemical potential, $\boldsymbol{\tau} = (\tau_x, \tau_y, \tau_z)$ is the vector of Pauli matrices in the band space, σ_0 and τ_0 are the identity matrices in the spin- and band space, respectively. Further, $\hat{c}_{\mathbf{k}} = \begin{bmatrix} \tilde{c}_{\uparrow,\mathbf{k}} \\ \tilde{c}_{\downarrow,\mathbf{k}} \end{bmatrix}$, with $\tilde{c}_{s,\mathbf{k}} = \begin{bmatrix} c_{1,s,\mathbf{k}} \\ c_{2,s,\mathbf{k}} \end{bmatrix}$, where $c_{m,s,\mathbf{k}}$ is a fermion annihilation operator in the band $m = 1, 2$ with spin $s = \uparrow, \downarrow$.

Due to the inherent multiband nature and to the presence of nonsymmorphic symmetries, the usual classification of the possible superconducting order parameters (based on point-group symmetries) in the effective single-band picture is insufficient for the 111 materials (see Supplementary Note 9 for details). Indeed, nonsymmorphic symmetries can lead to additional symmetry-imposed nodes along the high symmetry directions on the zone faces[37,38]. Even a loop supercurrent state[39], which has a uniform onsite singlet pairing and proposed to be realized in some of the fully-gapped TRS breaking superconductors, is not allowed in the case of 111 materials, because there are only two symmetrically distinct sites within a unit cell. However, we note that the two Fermi surfaces under consideration have large sections in the Brillouin zone which are almost parallel and close to each other (see Fig. 5b). Hence, to consistently explain the phenomenon of TRS breaking at T_c despite the presence of a full SC gap, we expect that an internally antisymmetric nonunitary triplet (INT) state[40,41], which features a uniform pairing between same spins in the two different bands, to become the dominant instability. In this state, the pairing potential matrix is $\hat{\Delta} = \hat{\Delta}_S \otimes \hat{\Delta}_B$, where $\hat{\Delta}_S$ and $\hat{\Delta}_B$ are the pairing potential matrices in the spin- and band-space, respectively. $\hat{\Delta}_B = i\tau_y$ gives the required fermionic antisymmetry. $\hat{\Delta}_S = (\mathbf{d}.\sigma)i\sigma_y$, where $\mathbf{d} = \Delta_0\boldsymbol{\eta}$, with $|\boldsymbol{\eta}|^2 = 1$, is the **d**-vector characterizing the triplet pairing state, which is nonunitary because $\mathbf{q} = i(\boldsymbol{\eta} \times \boldsymbol{\eta}^*) \neq 0$. Δ_0 is an overall pairing amplitude. Similarly, nonunitary triplet superconducting ground state was also proposed to be realized in the recently discovered 3D Dirac semimetals $LaNiGa_2$[42].

We compute the Bogoliubov quasiparticle energies $E_n(\mathbf{k})$, $n = 1, \ldots 4$ for the effective model in the INT ground state using the Bogoliubov-de-Gennes (BdG) formalism (see details also in Supplementary Note 9, Figs. 13–15, Tables 3 and 4). The thermodynamic properties are computed by assuming that the temperature dependence comes only from the pairing amplitude in the form $\Delta(T) = \Delta_0 \tanh\{1.82[1.018(T_c/T - 1)]^{0.51}\}$ and ignoring any weak temperature dependence of the **q**-vector. To reproduce the experimental specific-heat results for the three materials, three fitting parameters, namely, $\Delta_0/(k_BT_c)$, the direction of **d**-vector, and α had to be tuned to get the best fits in the weak-coupling limit (see Fig. 6). Note that, for all the three materials we can reproduce the specific-heat data rather well (especially at low temperatures) and the fitting process naturally preserves the trend of increasing ASOC strength in the 111 family. More importantly, the derived superconducting energy gaps are highly consistent with the values determined from TF-μSR measurements. The nonzero real vector **q**, found from the fits, points in different directions for the three materials and encodes the effective TRS-breaking field arising from spin-polarization caused by Cooper-pair migration due to the nonunitary nature of pairing[41].

DISCUSSION

According to ZF-μSR results in the 111 materials, the spontaneous magnetic fields or the magnetization in the superconducting state of LaPtSi or LaPtGe are much larger than in LaNiSi, here reflected in significantly larger variations of Λ_{ZF} between zero-temperature and T_c in the former two cases as compared to LaNiSi. Therefore, the TRS breaking effect is more prominent in the superconducting state of LaPtSi and LaPtGe than in LaNiSi (see Fig. 3). Previous ZF-μSR studies indicate that, although LaNiSi and LaPtSi exhibit an enhanced muon-spin relaxation rate at low temperatures, their $\Lambda_{ZF}(T)$ resembles a Curie-Weiss behavior [i.e., $\lambda_{ZF}(T) \propto T^{-1}$]. This, and the lack of a distinct anomaly in $\Lambda_{ZF}(T)$ across T_c[20], are inconsistent with a TRS breaking effect. In general, an enhanced muon-spin relaxation with Curie–Weiss features might be related to either intrinsic or to extrinsic spin fluctuations. As for the intrinsic case, a typical example is that of the ThFeAsN iron-based superconductor. It exhibits strong magnetic fluctuations at low temperatures (confirmed also by nuclear magnetic resonance measurements), which are reflected in a steadily increasing $\Lambda_{ZF}(T)$ as the temperature is lowered[43]. As for the extrinsic case, a typical example is that of the $ReBe_{22}$ multigap superconductor. Here, $\Lambda_{ZF}(T)$ increases remarkably with decreasing temperature due to tiny amounts of magnetic impurities, whose contribution is enhanced near zero temperature[28]. Conversely, in case of a truly

broken TRS—for instance, in the 111 materials we report here—Λ_{ZF} is almost independent of temperature for $T > T_c$, strongly suggesting that the enhanced Λ_{ZF} is induced by the spontaneous fields occurring in the superconducting state.

In LaPtGe, previous ZF-μSR data show similar features to our results (see Fig. 3f), i.e., a small yet clear difference in the ZF-μSR spectra between 0.3 and 4.5 K[21], the latter dataset referring to the normal state. However, the authors claimed that, the temperature-dependent σ_{ZF} and Λ_{ZF} exhibit no visible differences and, thus, a preserved TRS was concluded[21]. By contrast, our systematic ZF-μSR measurements suggest the presence of spontaneous magnetic fields, hence, the broken TRS in the superconducting state of LaPtGe. Such discrepancies in ZF-μSR results might be related to the different sample quality, purity, or disorder. For example, the previous study reports a residual resistivity $\rho_0 \sim 200\ \mu\Omega\,cm$[21], three times larger than that of current LaPtGe sample, $\rho_0 \sim 66\ \mu\Omega\,cm$ (see Supplementary Fig. 2 and Note 2). Moreover, the residual resistivity ratio of the current LaPtGe sample is twice larger than that of the previous sample. Nevertheless, to independently confirm the TRS breaking in the superconducting state of 111 materials, the use of other techniques, as e.g., Josephson tunneling, SQUID, or optical Kerr effect, is highly desirable. In particular, the optical Kerr effect, another very sensitive probe of spontaneous fields in unconventional superconductors, is renown for confirming TRS breaking in Sr_2RuO_4 and UPt_3[24,44]. In addition, to exclude disorder effects, search for possible non-*s*-wave behavior, and confirm the TRS breaking in the 111 materials, in the future, measurements on high-quality single crystals will clearly be helpful.

According to the Uemura plot[45], clearly, the 111 materials studied here lie in the band where there are other families of superconductors that are found to break TRS in the superconducting state (see details in Supplementary Fig. 16 and Note 10). Apart from the La-based 111 materials studied here, also the isostructural Th*T*Si compounds (with T = Co, Ni, Ir, and Pt) are superconductors (with critical temperatures between 2 and 6.5 K)[46,47]. Similar to the La-based cases, the Th-based materials, too, exhibit a large ASOC upon replacing the 3*d* Ni and Co with 5*d* Pt and Ir[48]. Recently, superconductivity with $T_c = 5.07$ K was reported in ThIrP, which also adopts a LaPtSi-type structure[49]. Therefore, it would be interesting to search for possible TRS breaking and, hence, unconventional superconductivity in these Th-based 111 materials. In addition, La-based 111 materials, in particular $LaNi_{1-x}Pt_xSi$, represent ideal candidate systems for investigating the effect of ASOC on spontaneous magnetization and unconventional superconductivity.

Generally, in noncentrosymmetric superconductors, the ASOC can induce a mixing of singlet and triplet states. However, in the 111 materials under consideration, it does more than that, becoming crucial in stabilizing even a purely triplet state. Moreover, the necessity of a dominant interband contribution to the ASOC in achieving a fully gapped spectrum in the INT state, further justifies the interband pairing in the superconducting state. We also note that the triplet **d**-vectors, obtained from analyses of the specific-heat data, correspond to a partially spin-polarized ($|\mathbf{q}| < 1 \neq 0$) superconducting state. In this case, the spontaneous magnetization results from a migration of Cooper pairs from the majority to the minority spin species[41].

The normal state of 111 materials has a non-trivial topology due to the Weyl nodal lines protected by the nonsymmorphic glide symmetry and TRS. Apart from the usual photoemission studies[1,2], the corresponding drumhead surface states can also be investigated by inspecting the correlation effects on the surfaces[50]. Since TRS is spontaneously broken at T_c, it is of interest to investigate the fate of the bulk nodal lines. Our results demonstrate that 111 materials represent a rare case of Weyl nodal-line semimetals, which break time-reversal symmetry in the superconducting state. As such, they epitomize the ideal system for investigating the rich interplay between the exotic properties of topological nodal-line fermions and unconventional superconductivity.

METHODS

Sample preparation

Polycrystalline LaNiSi, LaPtSi, and LaPtGe samples were prepared by arc melting La (99.9%, Alfa Aesar), Ni (99.98%, Alfa Aesar), Pt (99.9%, ChemPUR), Si (99.9999%, Alfa Aesar) and Ge (99.999%, Alfa Aesar) in high-purity argon atmosphere. To improve homogeneity, the ingots were flipped and re-melted more than five times. The as-cast ingots were then annealed at 800 °C for two weeks. The crystal structure and purity of the samples were checked using powder x-ray diffraction at room temperature using a Bruker D8 diffractometer with Cu K_α radiation. All three compounds crystallize in a tetragonal noncentrosymmetric structure with a space group $I4_1md$ (No. 109). The estimated lattice parameters are listed in the Supplementary Table 1.

Sample characterization

The magnetization, heat-capacity, and electrical-resistivity measurements were performed on a Quantum Design magnetic property measurement system (MPMS) and a physical property measurement system (PPMS). The lower critical field H_{c1} was determined by field-dependent magnetization measurements at various temperatures up to T_c, while the upper critical field H_{c2} was determined by measuring the temperature-dependent heat capacity under various magnetic fields, and by field-dependent magnetization at various temperatures.

μSR experiments

The μSR experiments were conducted at the general-purpose surface-muon (GPS) and at the low-temperature facility (LTF) instruments of the Swiss muon source (SμS) at Paul Scherrer Institut (PSI) in Villigen, Switzerland. Once implanted in a material, at a typical depth of ~0.3 mm, the spin-polarized positive muons (μ^+) act as microscopic probes of the local magnetic environment via the decay positrons, emitted preferentially along the muon-spin direction. The spatial anisotropy of the emitted positrons (i.e., the asymmetry signal) reveals the distribution of the local magnetic fields at the muon stopping sites[36,51]. For TF-μSR measurements, the applied magnetic field is perpendicular to the muon-spin direction, while for LF-μSR measurements, the magnetic field is parallel to the muon-spin direction. In both the TF- and LF-μSR cases, the samples were cooled in an applied magnetic field down to the base temperature (1.5 K for GPS and 0.02 K for LTF). Field cooling reduces flux pinning and ensures an almost ideal flux-line lattice. The μSR spectra were then collected upon heating. For the ZF-μSR measurements, to exclude the possibility of stray magnetic fields, the magnets were quenched before the measurements, and an active field-nulling facility was used to compensate for stray fields down to 1 μT.

Analysis of the μSR spectra

All the μSR data were analyzed by means of the `musrfit` software package[52]. In absence of applied external fields, in the nonmagnetic LaNiSi, LaPtSi, and LaPtGe, the relaxation is mainly determined by the randomly oriented nuclear magnetic moments. Therefore, their ZF-μSR spectra can be modeled by means of a phenomenological relaxation function, consisting of a combination of Gaussian- and Lorentzian Kubo-Toyabe relaxations[35,36]:

$$A_{ZF} = A_s\left[\frac{1}{3} + \frac{2}{3}\left(1 - \sigma_{ZF}^2 t^2 - \Lambda_{ZF} t\right) e^{\left(-\frac{\sigma_{ZF}^2 t^2}{2} - \Lambda_{ZF} t\right)}\right] + A_{bg}. \quad (2)$$

Here A_s and A_{bg} represent the initial muon-spin asymmetries for muons implanted in the sample and the sample holder, respectively. The σ_{ZF} and Λ_{ZF} represent the zero-field Gaussian- and Lorentzian relaxation rates, respectively. Since σ_{ZF} shows an almost temperature-independent behavior, the Λ_{ZF} values in Fig. 3a–c could be derived by fixing σ_{ZF} to its average value, i.e., $\sigma_{ZF}^{av} = 0.094$, 0.103, and 0.104 μs^{-1} for LaNiSi, LaPtSi, and LaPtGe, respectively (see details in Supplementary Fig. 7).

In the TF-μSR case, the time evolution of asymmetry was modeled by:

$$A_{TF}(t) = A_s \cos(\gamma_\mu B_s t + \phi) e^{-\sigma^2 t^2/2} + A_{bg} \cos(\gamma_\mu B_{bg} t + \phi). \quad (3)$$

Here A_s and A_{bg} are the same as in ZF-μSR. B_s and B_{bg} are the local fields sensed by implanted muons in the sample and the sample holder (i.e., silver plate), γ_μ is the muon gyromagnetic ratio, ϕ is the shared initial phase, and σ is a Gaussian relaxation rate reflecting the field distribution inside the sample. In the superconducting state, σ includes contributions from both the flux-line lattice (σ_{sc}) and a smaller, temperature-independent relaxation, due to the nuclear moments (σ_n, similar to σ_{ZF}). The former can be extracted by subtracting the σ_n in quadrature, i.e., $\sigma_{sc} = \sqrt{\sigma^2 - \sigma_n^2}$. Since σ_{sc} is directly related to the effective magnetic penetration depth and, thus, to the superfluid density ($\sigma_{sc} \propto 1/\lambda_{eff}^2 \sim \rho_{sc}$), the superconducting gap and its symmetry can be investigated by measuring the temperature-dependent σ_{sc}.

The effective penetration depth λ_{eff} could be calculated from σ_{sc} by considering the overlap of vortex cores[53]:

$$\sigma_{sc}(h) = 0.172\frac{\gamma_\mu \Phi_0}{2\pi}(1-h)[1+1.21(1-\sqrt{h})^3]\lambda_{eff}^{-2}. \quad (4)$$

Here, $h = H_{appl}/H_{c2}$, is the reduced magnetic field, where H_{appl} represents the applied external magnetic field and H_{c2} the upper critical fields. Values of the latter are reported in Supplementary Figs. 4–6. For the TF-μSR measurements we used $\mu_0 H_{appl} = 15$, 20, and 30 mT for LaNiSi, LaPtSi, and LaPtGe, respectively. Further details about the data analysis can be found in the Supplementary Note 5 and 6.

Superconducting gap symmetry

Since the 111 materials exhibit an almost temperature-independent superfluid density below $1/3T_c$, to extract the superconducting gap, the superfluid density $\rho_{sc}(T)$ of LaNiSi, LaPtSi, and LaPtGe was analyzed by using a fully-gapped *s*-wave model, generally described by:

$$\rho_{sc}(T) = \frac{\lambda_0^2}{\lambda_{eff}^2(T)} = 1 + 2\int_{\Delta(T)}^{\infty} \frac{E}{\sqrt{E^2-\Delta^2(T)}}\frac{\partial f}{\partial E}dE, \quad (5)$$

with $f = (1+e^{E/k_BT})^{-1}$ the Fermi function[54,55] and λ_0 the effective magnetic penetration depth at zero temperature. The temperature evolution of the superconducting energy gap follows $\Delta(T) = \Delta_0 \tanh\{1.82[1.018(T_c/T-1)]^{0.51}\}$, where Δ_0 is the gap value at zero temperature[56].

Theoretical analysis

We use the Bogoliubov-de-Gennes formalism to compute the quasiparticle energy bands for the minimal two-band model in the INT state[8]. Here, we assume the temperature dependence comes only from the pairing amplitude. The Bogoliubov quasiparticle energy bands $E_n(\mathbf{k})$; $n = 1\ldots4$ are used to compute the specific heat by means of the formula:

$$C = \sum_{n,\mathbf{k}} \frac{k_B\beta^2}{2}\left[E_n(\mathbf{k}) + \beta\frac{\partial E_n(\mathbf{k})}{\partial\beta}\right]E_n(\mathbf{k})\ \mathrm{sech}^2\left[\frac{\beta E_n(\mathbf{k})}{2}\right] \quad (6)$$

where $\beta = \frac{1}{k_BT}$ and k_B is the Boltzmann constant. Further details about the theoretical analysis can be found in the Supplementary Note 9.

DATA AVAILABILITY

All the data needed to evaluate the reported conclusions are presented in the paper and/or in the Supplementary Material. Additional data related to this paper may be requested from the authors. The μSR data were generated at the SμS (Paul Scherrer Institut, Switzerland). Derived data supporting the results of this study are available from the corresponding authors or beamline scientists. The `musrfit` software package is available online free of charge at http://lmu.web.psi.ch/musrfit/technical/index.html.

Received: 3 November 2021; Accepted: 18 February 2022;
Published online: 25 March 2022

REFERENCES

1. Armitage, N. P., Mele, E. J. & Vishwanath, A. Weyl and Dirac semimetals in three-dimensional solids. *Rev. Mod. Phys.* **90**, 015001 (2018).
2. Lv, B. Q., Qian, T. & Ding, H. Experimental perspective on three-dimensional topological semimetals. *Rev. Mod. Phys.* **93**, 025002 (2021).
3. Zhang, P., Yuan, H. & Cao, C. Electron-phonon coupling and nontrivial band topology in noncentrosymmetric superconductors LaNiSi, LaPtSi, and LaPtGe. *Phys. Rev. B* **101**, 245145 (2020).
4. Lee, W. H., Yang, F. A., Shih, C. R. & Yang, H. D. Crystal structure and superconductivity in the Ni-based ternary compound LaNiSi. *Phys. Rev. B* **50**, 6523–6525 (1994).
5. Kneidinger, F. et al. Synthesis, characterization, electronic structure, and phonon properties of the noncentrosymmetric superconductor LaPtSi. *Phys. Rev. B* **88**, 104508 (2013).
6. Evers, J., Oehlinger, G., Weiss, A. & Probst, C. Superconductivity of LaPtSi and LaPtGe. *Solid State Commun.* **50**, 61–62 (1984).
7. Annett, J. F. Symmetry of the order parameter for high-temperature superconductivity. *Adv. Phys.* **39**, 83–126 (1990).
8. Sigrist, M. & Ueda, K. Phenomenological theory of unconventional superconductivity. *Rev. Mod. Phys.* **63**, 239–311 (1991).
9. Ghosh, S. K. et al. Recent progress on superconductors with time-reversal symmetry breaking. *J. Phys.: Condens. Matter* **33**, 033001 (2020).
10. Hillier, A. D., Quintanilla, J. & Cywinski, R. Evidence for time-reversal symmetry breaking in the noncentrosymmetric superconductor $LaNiC_2$. *Phys. Rev. Lett.* **102**, 117007 (2009).
11. Barker, J. A. T. et al. Unconventional superconductivity in La_7Ir_3 revealed by muon spin relaxation: introducing a new family of noncentrosymmetric superconductor that breaks time-reversal symmetry. *Phys. Rev. Lett.* **115**, 267001 (2015).
12. Singh, R. P. et al. Detection of time-reversal symmetry breaking in the noncentrosymmetric superconductor Re_6Zr using muon-spin spectroscopy. *Phys. Rev. Lett.* **112**, 107002 (2014).
13. Shang, T. et al. Time-reversal symmetry breaking in Re-based superconductors. *Phys. Rev. Lett.* **121**, 257002 (2018).
14. Shang, T. et al. Time-reversal symmetry breaking in the noncentrosymmetric Zr_3Ir superconductor. *Phys. Rev. B* **102**, 020503(R) (2020).
15. Smidman, M., Salamon, M. B., Yuan, H. Q. & Agterberg, D. F. Superconductivity and spin–orbit coupling in non-centrosymmetric materials: a review. *Rep. Prog. Phys.* **80**, 036501 (2017).
16. Bauer, E. & Sigrist, M. (eds.) *Non-Centrosymmetric Superconductors*, vol. 847 (Springer, 2012).
17. Sato, M. & Ando, Y. Topological superconductors: a review. *Rep. Prog. Phys.* **80**, 076501 (2017).
18. Qi, X.-L. & Zhang, S.-C. Topological insulators and superconductors. *Rev. Mod. Phys.* **83**, 1057–1110 (2011).
19. Kallin, C. & Berlinsky, J. Chiral superconductors. *Rep. Prog. Phys.* **79**, 054502 (2016).
20. Sajilesh, K. P., Singh, D., Hillier, A. D. & Singh, R. P. Probing nodeless superconductivity in La *M*Si (*M* = Ni, Pt) using muon-spin rotation and relaxation. *Phys. Rev. B* **102**, 094515 (2020).
21. Sajilesh, K. P., Singh, D., Biswas, P. K., Hillier, A. D. & Singh, R. P. Superconducting properties of the noncentrosymmetric superconductor LaPtGe. *Phys. Rev. B* **98**, 214505 (2018).
22. Luke, G. M. et al. Muon spin relaxation in UPt_3. *Phys. Rev. Lett.* **71**, 1466–1469 (1993).
23. de Réotier, P. D. et al. Absence of zero field muon spin relaxation induced by superconductivity in the B phase of UPt_3. *Phys. Lett. A* **205**, 239–243 (1995).
24. Schemm, E. R., Gannon, W. J., Wishne, C. M., Halperin, W. P. & Kapitulnik, A. Observation of broken time-reversal symmetry in the heavy-fermion superconductor UPt_3. *Science* **345**, 190–193 (2014).
25. Zhu, X., Yang, H., Fang, L., Mu, G. & Wen, H.-H. Upper critical field, Hall effect and magnetoresistance in the iron-based layered superconductor $LaFeAsO_{0.9}F_{0.1-\delta}$. *Supercond. Sci. Technol.* **21**, 105001 (2008).
26. Werthamer, N. R., Helfand, E. & Hohenberg, P. C. Temperature and purity dependence of the superconducting critical field, H_{c2}. III. Electron spin and spin–orbit effects. *Phys. Rev.* **147**, 295–302 (1966).
27. Gurevich, A. Iron-based superconductors at high magnetic fields. *Rep. Prog. Phys.* **74**, 124501 (2011).
28. Shang, T. et al. Enhanced T_c and multiband superconductivity in the fully-gapped $ReBe_{22}$ superconductor. *New J. Phys.* **21**, 073034 (2019).
29. Shang, T. et al. Multigap superconductivity in the Mo_5PB_2 boron-phosphorus compound. *New J. Phys.* **22**, 093016 (2020).
30. Amato, A. Heavy-fermion systems studied by μSR technique. *Rev. Mod. Phys.* **69**, 1119–1180 (1997).
31. Luke, G. M. et al. Time-reversal symmetry-breaking superconductivity in Sr_2RuO_4. *Nature* **394**, 558–561 (1998).
32. Aoki, Y. et al. Time-reversal symmetry-breaking superconductivity in heavy-fermion $PrOs_4Sb_{12}$ detected by muon-spin relaxation. *Phys. Rev. Lett.* **91**, 067003 (2003).
33. Shang, T. et al. Nodeless superconductivity and time-reversal symmetry breaking in the noncentrosymmetric superconductor $Re_{24}Ti_5$. *Phys. Rev. B* **97**, 020502 (2018).

34. Shang, T. et al. Simultaneous nodal superconductivity and time-reversal symmetry breaking in the noncentrosymmetric superconductor CaPtAs. *Phys. Rev. Lett.* **124**, 207001 (2020).
35. Kubo, R. & Toyabe, T. *Magnetic Resonance and Relaxation*. (North-Holland, 1967).
36. Yaouanc, A. & de Réotier, P. D. *Muon Spin Rotation, Relaxation, and Resonance: Applications to Condensed Matter*. (Oxford University Press, Oxford, 2011).
37. Sumita, S. & Yanase, Y. Unconventional superconducting gap structure protected by space group symmetry. *Phys. Rev. B* **97**, 134512 (2018).
38. Sumita, S., Nomoto, T., Shiozaki, K. & Yanase, Y. Classification of topological crystalline superconducting nodes on high-symmetry lines: Point nodes, line nodes, and Bogoliubov Fermi surfaces. *Phys. Rev. B* **99**, 134513 (2019).
39. Ghosh, S. K., Annett, J. F. & Quintanilla, J. Time-reversal symmetry breaking in superconductors through loop supercurrent order. *New J. Phys.* **23**, 083018 (2021).
40. Weng, Z. F. et al. Two-gap superconductivity in $LaNiGa_2$ with nonunitary triplet pairing and even parity gap symmetry. *Phys. Rev. Lett.* **117**, 027001 (2016).
41. Ghosh, S. K. et al. Quantitative theory of triplet pairing in the unconventional superconductor $LaNiGa_2$. *Phys. Rev. B* **101**, 100506 (2020).
42. Jackson, R. et al. Dirac lines and loop at the Fermi level in the time-reversal symmetry breaking superconductor $LaNiGa_2$. *Commun. Phys.* **5**, 22 (2022).
43. Shiroka, T. et al. High-T_c superconductivity in undoped ThFeAsN. *Nat. Commun.* **8**, 156 (2017).
44. Xia, J., Maeno, Y., Beyersdorf, P. T., Fejer, M. M. & Kapitulnik, A. High resolution polar Kerr effect measurements of Sr_2RuO_4: evidence for broken time-reversal symmetry in the superconducting state. *Phys. Rev. Lett.* **97**, 167002 (2006).
45. Uemura, Y. J. et al. Basic similarities among cuprate, bismuthate, organic, Chevrel-phase, and heavy-fermion superconductors shown by penetration-depth measurements. *Phys. Rev. Lett.* **66**, 2665 (1991).
46. Domieracki, K. & Kaczorowski, D. Superconductivity in non-centrosymmetric ThNiSi. *J. Alloy. Compd.* **731**, 64–69 (2018).
47. Zhong, W. X., Ng, W. L., Chevalier, B., Etourneau, J. & Hagenmuller, P. Structural and electrical properties of new silicides: $ThCo_xSi_{2-x}$ ($0 \leq x \leq 1$) and ThTSi (T = Ni, Pt). *Mater. Res. Bull.* **20**, 1229–1238 (1985).
48. Ptok, A. et al. Electronic and lattice properties of noncentrosymmetric superconductors Th*T*Si (*T* = Co, Ir, Ni, and Pt). *Phys. Rev. B* **100**, 165130 (2019).
49. Xiao, G. et al. Superconductivity and strong spin-orbit coupling in a new noncentrosymmetric compound ThIrP. *Sci. China Phys. Mech. Astron.* **64**, 107411 (2021).
50. Liu, J. & Balents, L. Correlation effects and quantum oscillations in topological nodal-loop semimetals. *Phys. Rev. B* **95**, 075426 (2017).
51. Blundell, S. J. Spin-polarized muons in condensed matter physics. *Contemp. Phys.* **40**, 175–192 (1999).
52. A. Suter, A. & Wojek, B. M. Musrfit: a free platform-independent framework for μSR data analysis. *Phys. Procedia* **30**, 69–73 (2012).
53. Brandt, E. H. Properties of the ideal Ginzburg-Landau vortex lattice. *Phys. Rev. B* **68**, 054506 (2003).
54. Tinkham, M. *Introduction to Superconductivity* 2nd edn. (Dover Publications, 1996).
55. Prozorov, R. & Giannetta, R. W. Magnetic penetration depth in unconventional superconductors. *Supercond. Sci. Technol.* **19**, R41–R67 (2006).
56. Carrington, A. & Manzano, F. Magnetic penetration depth of MgB_2. *Phys. C* **385**, 205–214 (2003).

ACKNOWLEDGEMENTS

We acknowledge the allocation of beam time at SμS (GPS and LTF spectrometers). We thank Peiran Zhang and Chao Cao for sharing the band structure data for LaNiSi, and other related discussions. T.S. acknowledges support by the Natural Science Foundation of Shanghai (Grant Nos. 21ZR1420500 and 21JC1402300). S.K.G., J.F.A., and J.Q. acknowledge support by EPSRC through the project "Unconventional Superconductors: New paradigms for new materials" (Grant Refs. EP/P00749X/1 and EP/P007392/1). S.K.G. also acknowledges the Leverhulme Trust for support through the Leverhulme early-career fellowship. This work was also supported by the Swiss National Science Foundation (Grant Nos. 200021_188706, 200021_169455, 206021_139082). M.S. and H.Q.Y. acknowledge the National Key R&D Program of China (Grant No. 2017YFA0303100), the National Natural Science Foundation of China (Grant Nos. 11874320, 12034017, and 11974306), the Key R&D Program of Zhejiang Province, China (Grant No. 2021C01002), and the Zhejiang Provincial Natural Science Foundation of China (Grant No. R22A0410240).

AUTHOR CONTRIBUTIONS

T.S., S.K.G., M.S., H.Q.Y., J.Q., and T.Sh. conceived and led the project. T.S., S.K.G., and M.S. contributed equally to this work. T.S., D.J.G., and E.P. synthesized the samples. T.S., T.Sh., and C.B. performed the μSR measurements. S.K.G. performed the theoretical analysis with advice from J.Q. and J.F.A. T.S., A.W., W.X., Y.C., M.O.A., M.N., and M.M. measured the electrical resistivity, heat capacity, and magnetization. T.S. analyzed all the experimental data. T.S., S.K.G., and M.S. wrote the paper with input from all the co-authors.

COMPETING INTERESTS

The authors declare no competing interests

ADDITIONAL INFORMATION

Supplementary information The online version contains supplementary material available at https://doi.org/10.1038/s41535-022-00442-w.

Correspondence and requests for materials should be addressed to Huiqiu Yuan, Jorge Quintanilla or Toni Shiroka.

Reprints and permission information is available at http://www.nature.com/reprints

Publisher's note Springer Nature remains neutral with regard to jurisdictional claims in published maps and institutional affiliations.